Internal Gravity Wave Generation and Hydrodynamic Instability

B. R. SUTHERLAND, C. P. CAULFIELD, AND W. R. PELTIER

Department of Physics, University of Toronto, Toronto, Ontario, Canada

(Manuscript received 27 July 1993, in final form 9 February 1994)

ABSTRACT

Two mechanisms are proposed whereby internal gravity waves (IGW) may radiate from a linearly unstable region of Boussinesq parallel flow that is characterized in the far field by constant horizontal velocity and Brunt–Väisälä frequency. Through what is herein referred to as "primary generation," IGW may be directly excited by linear instability of the initial-state parallel shear flow. Characteristically, these waves propagate with horizontal phase speed and wavenumber equal to that of the most unstable mode of linear stability theory. Through the second mechanism, referred to as "secondary generation," IGW may be excited via nonlinear modification of the initial instability into a form that couples strongly to a large amplitude outgoing internal wave field. The authors propose that the primary generation of IGW may occur provided a penetration condition, which is derived on the basis of linear theory, is satisfied. The penetration condition provides a limit on the growth rate of a disturbance of any particular frequency that is capable of propagating into the far field. This hypothesis is supported by a sequence of representative nonlinear numerical simulations in two spatial dimensions for both free mixing layer and jet flows with horizontal velocity profiles $U(z) = \tanh(z)$ and $U(z) = \text{sech}^2(z)$, respectively. For the purpose of these analyses, the fluid density is taken to be such that the square of the Brunt–Väisälä frequency is given by $N^2(z) = J \tanh^2(z/R)$. Such stratification allows both for the development of large-scale eddies in the region of low static stability and, in the far field where $N^2 \approx J$ is positive and approximately constant, for the radiation of a broad frequency spectrum of IGW.

---

1. Introduction

The momentum deposition associated with the "breaking" of internal gravity waves (hereafter referred to as IGW) in the middle and upper atmosphere is believed to constitute a significant forcing of the mean flow, as first pointed out by Hines (1960) and Hodges (1969) and further examined by Lindzen (1981). In the absence of internal wave forcing, for example, Geller (1983) has shown through numerical experiments that the extrema of temperature at the summer and winter stratopause/mesopause are overpredicted. Irregular motions such as the equatorial quasi-biennial oscillation are also understood to be driven in part by mixed Rossby–IGW that originate in the troposphere (Lindzen and Holton 1968; Holton and Lindzen 1972; Takahashi and Holton 1991). Recent analyses of observational data by Nastrom and Fritts (1992) and Fritts and Nastrom (1992) have attempted to identify the various tropospheric sources of IGW. The most intense source of mixing according to these analyses is by IGW generated by topographic forcing. They showed, however, that IGW that radiate from convective or frontal systems or from instabilities of the jet stream may also be responsible for large vari-

ances in the observed mean zonal and meridional velocity fields and in the mean temperature field. The mechanism by which IGW are generated by stratified flow over surface topography has been examined in detail by many authors, including Lilly (1971), Peltier and Clark (1979), and Durran and Klemp (1987). Though recent progress has been made in the understanding of the mechanism by which IGW are generated by convective mixing (Clark et al. 1986; Fovell 1992), the efficient generation of IGW by nonstationary sources such as wind shear has never been clearly demonstrated. Indeed, the analysis of McIntyre and Weissman (1978) has often been misconstrued as implying that linear parallel shear instability cannot lead to the direct emission of such waves.

The possible excitation of IGW by eddies that develop in an unstable shear layer has been examined previously in the context of linear theory by Drazin et al. (1979), who classified as "unbound" those (neutrally stable) modes that propagate at infinity and are modified by shear. Their analysis included an examination of IGW modified by coupling with unstable modes of the Bickley jet and hyperbolic tangent shear layer in fluid with N^2 constant. However, these authors focused primarily on the nature of modes with horizontal phase speeds greater than the maximum velocity or less than the minimum velocity of the parallel flow. Such waves clearly cannot be generated spontaneously by instability processes (Howard 1961). Fritts (1982)

Corresponding author address: Dr. W. R. Peltier, Department of Physics, University of Toronto, Toronto, Ontario M5S 1A7, Canada.
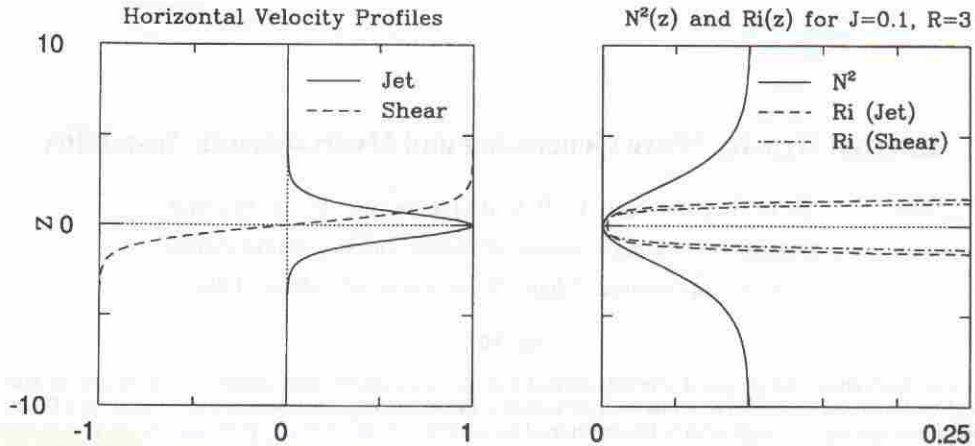
FIG. 1. Vertical profiles of (a) horizontal velocity $U(z)$ and (b) squared Brunt–Väisälä frequency $N^2(z)$ and local Richardson number. The jet flow profile (solid curve) is of the Bickley form, $\text{sech}^2(z)$, and the shear flow profile (dashed curve) is of the form $\tanh(z)$; N^2 is given by $J\tanh^2(z/R)$ in which the case $J = 0.1$ and $R = 3$ is shown above (solid curve). The local Richardson number calculated for this form of N^2 is shown for the jet (dashed curve) and the shear (dot–dashed curve).

examined various unstable modes of hyperbolic tangent shear flow with N^2 constant and showed that one family of such modes is vertically propagating above the shear layer. The growth rate of these modes is much smaller than that of the most unstable mode, however, and there is the important issue as to whether any significant IGW radiation may be excited in this circumstance. Since a direct linear mechanism for emission appeared not to be available, a number of nonlinear mechanisms have been proposed by Fritts (1982, 1984) and Chimonas and Grant (1984), for example, whereby propagating disturbances may be excited by resonant interaction with Kelvin modes of similar wavelength. The nonlinear generation of IGW by subharmonic excitation, such as vortex pairing, was in fact proposed earlier by Davis and Peltier (1979). Recently, however, in the context of a sequence of high-resolution numerical simulations, Sutherland and Peltier (1994) observed the radiation of large amplitude IGW on the flanks of a jet flow in fluid with variable $N^2(z; J, R)$ [J and R are constant parameters—see Eq. (1)]. These waves were apparently directly excited in some parameter regimes as a consequence of linear instability of the basic state, while in other parameter regimes emission was observed to occur through nonlinear mechanisms.

Since the initial intrusion of waves into a statically and dynamically stable region constitutes a linear process, linear theory may be employed to predict the conditions under which the incident waves may pass unretarded through the region. Some new results from linear theory applied to an unstable parallel flow of Boussinesq fluid with constant horizontal velocity U_∞ and Brunt–Väisälä frequency N_∞ above some level z_1 are presented in section 2. Therein, a "penetration condition" is derived that we propose may be used to distinguish two mechanisms by which radiating waves may be generated.

As pointed out by McIntyre and Weissman (1978) and Davis and Peltier (1979), the generation of IGW by eddies that develop from instability of the mean flow might be expected to involve nonlinear interactions, and there is some question as to the extent to which linear theory may be applicable. For this reason, the nonlinear evolution of two-dimensional unstable jet flows and shear flows in variable N^2 fluid will be herein simulated numerically, the results of which are presented in section 3. The vertical profile of horizontal velocity of the jet flow will be taken as $U(z) = \text{sech}^2(z)$ (the so-called Bickley jet) and the shear flow considered here will be of the $\tanh(z)$ form. The velocity profiles for these flows are shown in Fig. 1a. As in Sutherland and Peltier (1994), the vertical variation of background density is taken to be such that N^2 is of the nondimensional form

$$N^2(z) = J\tanh^2(z/R),\qquad (1)$$

in which R is the scale of the density variation and J is a characteristic value of N^2. The vertical profile of N^2 is the solid curve shown in Fig. 1b for a particular choice of parameters. This form is deliberately chosen so that eddies may develop in the region of low static stability and force IGW in the ambient stratified fluid. It is a particular example of the profile for N^2 considered by Lott et al. (1992), who found analytical expressions for the marginal curves of hyperbolic tangent shear flow. In Sutherland and Peltier (1994), it is argued that initial mixing processes in shear flows in the atmosphere may naturally adjust the background density variation so that N^2 becomes small over the vertical extent of the layer. If the large-scale forcing that originally induced the shear layer was to reinforce it fol-

lowing an initial episode of mixing, then the initial conditions that we assume for our analyses would be entirely expected.

Numerical simulations have been conducted using the above set of initial conditions for two jet flows, for which the penetration condition is not satisfied (is satisfied) by the most unstable mode of linear theory, and therefore, IGW are not expected (are expected) to be excited directly by the instability. In both cases, wave packets of IGW with approximately the same horizontal wavenumber and phase speed as the most unstable mode of linear stability theory are observed to propagate vertically away from either flank of the jet. The energy of the radiating waves is equally partitioned between kinetic and available potential forms, a feature that is characteristic of neutrally propagating waves.

The results for these jet simulations are compared with corresponding simulations for shear flow. In one case, the most unstable mode does not satisfy the penetration condition and the intrusion into the far field of IGW of the same horizontal wavenumber as the most unstable mode is not observed. Instead, waves with twice the horizontal wavelength are observed to radiate, corroborating the viability of the nonlinear generation mechanism first suggested by Davis and Peltier (1979). In a second simulation of shear flow, the penetration condition is satisfied by the most unstable mode and waves of the same horizontal wavelength as the most unstable mode continuously radiate away from the region of strong shear. In this case it is shown that the energy density of radiated waves and the vertical flux of horizontal pseudomomentum across a fixed level outside the mixing region are significantly larger than those of the other three cases investigated. In particular, we believe this last case to be representative of many realizable atmospheric flows and that intense emission of this kind may explain the source of much of the IGW activity that is actually observed in the middle and upper atmosphere.

2. Linear theory

The governing equations of the linear stability problem are expressed in nondimensional form with respect to characteristic length and velocity scales $\mathscr{L}$ and $\mathscr{U}$, respectively. Here $\mathscr{L}$ may be identified with an appropriate measure of the depth over which the velocity of the jet or shear layer varies, and $\mathscr{U}$ may be identified with the maximum velocity of the flow. The horizontal velocity u and vertical velocity w are then expressed in nondimensional form by the substitutions $u \to \mathscr{U}u$ and $w \to \mathscr{U}w$. In the Boussinesq approximation, the background density is assumed to vary on a length scale $\mathscr{H} \gg \mathscr{L}$. The density fluctuation field ρ' is expressed in nondimensional form by the substitution $\rho' \to (\mathscr{L}\rho_0/\mathscr{H})\rho'$ in which ρ_0 is a measure of the background density at some reference level.

It is now well known that a flow with vertical profile of horizontal velocity $U = \bar{U}(z)$ and of density $\rho = \bar{\rho}(z)$ may give rise to the growth of unstable perturbations, the necessary condition for linear normal mode instability being given by the so-called Miles–Howard theorem (Miles 1961; Howard 1961). This seminal result follows through consideration of the stability of a two-dimensional, stratified flow in the Boussinesq approximation to small perturbations in velocity, pressure, and density. These perturbations may be denoted by $\mathbf{u}'$, p', and ρ', respectively. Since the flow is two-dimensional, we may express the x and z components of the velocity perturbation in terms of derivatives of a streamfunction $\psi(x, z)$. For the purpose of a conventional modal stability analysis, the disturbance may be assumed to be periodic in the streamwise direction allowing ψ to be resolved into Fourier components with horizontal wavenumber α, (possibly complex) phase speed c, and amplitude that varies with z. Explicitly, $\psi(x, z) = \phi(z) \exp[i\alpha(x - ct)]$. Substituting these quantities into the basic equations of motion and keeping only first-order terms, it is found that the complex amplitude $\phi(z)$ satisfies the classical Taylor–Goldstein equation (e.g., see Drazin and Reid 1981, section 44.2):

$$\phi'' + \gamma^2 \phi = 0, \tag{2}$$

in which

$$\gamma^2 = \frac{N^2}{(\bar{U} - c)^2} - \frac{\bar{U}''}{(\bar{U} - c)} - \alpha^2. \tag{3}$$

Here N is the Brunt–Väisälä frequency, defined as $N^2 = -J(d\bar{\rho}/dz)$ in which $J = (g/\mathscr{H})(\mathscr{L}/\mathscr{U})^2$ is the bulk Richardson number and g is the acceleration due to gravity. It is supposed that the flow is stably stratified so that N^2 is everywhere nonnegative.

Methods for the solution of the eigenvalue problem posed by Eqs. (2) and (3), along with suitable boundary conditions, have been discussed by many authors (e.g., Drazin and Reid 1981), and it is not the focus of the analysis to be presented herein. Rather, we consider the form of the eigenfunction over a vertical range in which $\bar{U}(z)$ and $N^2(z)$ are constant and we examine the condition that this form imposes on the sustained radiation of IGW. Supposing $\bar{U}(z) = U_0$ and $N^2(z) = N_0^2$ are constant over a range $z \in [z_1, z_2]$, then (2) is the wave equation with solution

$$\phi(z) = C_+ e^{i\gamma_0 z} + C_- e^{-i\gamma_0 z}, \tag{4}$$

in which $C_\pm$ are constants and the vertical wavenumber γ_0, from Eq. (3), is defined by

$$\gamma_0^2 = \frac{N_0^2}{(U_0 - c)^2} - \alpha^2. \tag{5}$$

Anticipating the imposition of boundary conditions, the branch of the square root defining γ_0 is taken so that

$$\arg(\gamma_0) \in (0, \pi]. \tag{6}$$

For neutral waves (for which c is real), Eq. (5) is the dispersion relationship for internal gravity waves in a nonrotating Boussinesq fluid, usually written in the form

$$\Omega^2 = N_0^2 \cos^2\Theta, \tag{7}$$

in which $\cos^2\Theta = \alpha^2/(\alpha^2 + \gamma_0^2)$ and $\Omega^2 = \alpha^2(U_0 - c)^2$. In this form, Θ represents the angle that the wavenumber vector makes with the horizontal and $\Omega = \alpha(c - U_0)$ is the Doppler-shifted frequency of the wave with respect to the background flow. By convention it is assumed that α is positive and Ω is positive for $c > U_0$. If $\Omega \leq N_0$ so that $\gamma_0^2 \geq 0$, then γ_0 is real [by Eq. (6), $\gamma_0 \leq 0$] and Eq. (4) represents a general propagating wave solution. If $\Omega > N_0$ so that $\gamma_0^2 < 0$, then γ_0 is pure imaginary (the root lying in the upper half complex plane) and Eq. (4) corresponds to a superposition of two evanescent waves. If the amplitude of the waves grows in time, then c and hence γ_0 will, in general, have both real and imaginary parts. Explicitly, the vertical wavenumber in the range $[z_1, z_2]$ may be written in the form $\gamma_0 = \gamma_{0r} + i\gamma_{0i}$.

With these comments in mind, the propagation of IGW is considered in a flow that is unbounded above and for which, above some level (say, $z \geq z_1$), the horizontal velocity $U = U_\infty$ and the Brunt–Väisälä frequency $N = N_\infty$ are constant. This region will be referred to hereafter as $\mathcal{R}_1$, consistent with the nomenclature in McIntyre and Weissman (1978). (The arguments that follow may easily be extended to the case of downward penetration of waves into a region of constant U and N^2 that is unbounded below.) In what follows, it will be unnecessary to specify whether or not the flow is bounded below, and no particular form for either $U(z)$ or $N^2(z)$ will be assumed for the region below z_1, though the background flow below $\mathcal{R}_1$ is assumed to be unstable and thus capable of generating disturbances in $\mathcal{R}_1$ spontaneously. Because of the choice of branch cut in the definition of γ_0 [Eq. (6)], it is clear that the form of a linear normal mode in $\mathcal{R}_1$ is given by Eq. (4) with $C_- = 0$. This follows by requiring that $|\phi(z)|$ is bounded (does not diverge for large z) when γ_0 is complex and by the requirement for upward energy propagation if γ_0 is real. Drazin et al. (1979) refer to the latter case as "unbounded." As a simple corollary, since γ_{0i} is positive definite for an unstable mode (for which c is complex), it is concluded that all unstable modes are bounded. Only neutral modes for which $\Omega \leq N_\infty$ (corresponding to propagating wave disturbances) are unbounded.

In developing a condition for sustained radiation into $\mathcal{R}_1$ due to an instability below $\mathcal{R}_1$ with phase speed $c = c_r + ic_i$, McIntyre and Weissman (1978) developed the phase speed condition (referred to hereafter as the PSC) requiring that $U_\infty - N_\infty/\alpha < c_r < U_\infty + N_\infty/\alpha$ for some wavenumber $\alpha > 0$. They further estimated the length scale L (the penetration depth) of penetration of

the instability into $\mathcal{R}_1$ as a function of the growth rate $\Omega_i = \alpha c_i$ by

$$L \leq \frac{1}{\alpha}\frac{|\Omega_r|}{\Omega_i}. \tag{8}$$

This upper bound leads the authors to conclude that the development of disturbances which satisfy the PSC are apparently trapped (as opposed to the real trapping of waves not satisfying the PSC) during the linear growth stage. Even in cases for which the PSC is satisfied, they propose that a nonlinear treatment would be required to judge the effectiveness of an instability as a radiator. This conclusion may be overly pessimistic, however, since a detailed analysis of the dispersion relationship for growing disturbances leads us to define a penetration condition that is a generalization of the PSC and that, we demonstrate, does indeed predict the effectiveness of wave radiation by unstable growing modes on the basis of linear theory. The penetration condition is derived in what follows.

A measure of the intrusion into $\mathcal{R}_1$ of IGW of vertical wavenumber γ_r and penetration depth $1/\gamma_i$ may be provided by $\mathcal{D} = \gamma_r/\gamma_i$, referred to hereafter as the penetration ratio (which is the ratio of the length scale on which the amplitude of the wave in $\mathcal{R}_1$ will be diminished by a factor e to the wavelength of the wave). We note that $\mathcal{D}$ is positive (negative) if the horizontal component of the phase speed of a growing wave in $\mathcal{R}_1$ is less than (greater than) the speed of the background flow in $\mathcal{R}_1$. This result follows from the condition for upward energy propagation. If $|\mathcal{D}| > 1$, the penetration condition is said to be satisfied and, since the disturbance is associated with some undulant vertical motion over one penetration depth, it is supposed that waves radiate significantly into $\mathcal{R}_1$. Together with the form of the dispersion relation for temporally growing disturbances, the penetration condition imposes a restriction on the growth rate for radiating waves.

Dividing Eq. (5) by α^2 we obtain

$$\Gamma^2 = \frac{N_\infty^2}{\Omega^2} - 1 \tag{9}$$

in which $\Gamma = \gamma_0/\alpha$. Expanding Eq. (9) for complex Γ and Ω and matching real and imaginary parts, it is clear that

$$\Gamma_r^2 - \Gamma_i^2 = N_\infty^2\frac{(\Omega_r^2 - \Omega_i^2)}{|\Omega|^4} - 1 \tag{10}$$

and

$$\Gamma_r\Gamma_i = -N_\infty^2\frac{\Omega_r\Omega_i}{|\Omega|^4}. \tag{11}$$

Assuming that the intrusion of IGW into $\mathcal{R}_1$ is a linear process, $\mathcal{D}$ can be found in terms of the frequency and growth rate of the wave by dividing Eq. (11) by Eq. (10) to obtain

$$\mathscr{D}^2 - 2B\mathscr{D} - 1 = 0, \qquad (12)$$

in which

$$B = \frac{1}{2}\frac{1}{\Omega_r \Omega_i}\left(\frac{1}{N_\infty^2}\,|\Omega|^4 - \Omega_r^2 + \Omega_i^2\right). \qquad (13)$$

Explicitly solving Eq. (12) for $\mathscr{D}$, we have the roots

$$\mathscr{D}_\pm = B \pm \sqrt{B^2 + 1}. \qquad (14)$$

If $B > 0$ ($B < 0$), the penetration condition is $\mathscr{D}_+ > 1$ ($\mathscr{D}_- < -1$), and $|\mathscr{D}_\pm| = 1$ if and only if $B = 0$.

For finite and nonzero Ω_r and Ω_i, the critical condition $B = 0$ is equivalent to

$$\frac{1}{N_\infty^2}(\Omega_r^2 + \Omega_i^2)^2 - \Omega_r^2 + \Omega_i^2 = 0, \qquad (15)$$

which implicitly defines the critical growth rate Ω_i for IGW radiation as a function of the Doppler-shifted frequency Ω_r. The square of the critical growth rate is shown by the heavy curve in Fig. 2. Also shown in Fig. 2 are curves for which $|\mathscr{D}| = 2$ and 3, the curves asymptotically approaching the Ω_r^2 axis in the range $0 < \Omega_r < J^{1/2}$ for successively larger values of $|\mathscr{D}|$. Where $|\mathscr{D}| > 1$ in Fig. 2, values of Ω_r and Ω_i are such that $B < 0$ ($B > 0$) if the product $\Omega_r\Omega_i > 0$ ($\Omega_r\Omega_i < 0$). The dotted line extending from the peak of the curve $|\mathscr{D}| = 1$ to the Ω_r^2 axis represents values of $\Omega_r^2 = \frac{1}{4}(\Omega_i^2 + 1)$ for which the penetration ratio is greatest for a disturbance of a given growth rate. From Fig. 2, limits on the growth rate and frequency of radiating waves are apparent. Internal waves do not radiate into $\mathscr{R}_1$ if the rate of growth of the disturbance exceeds $\sigma_{max} = N_\infty/8^{1/2}$. The frequency corresponding to this maximum is $N_\infty(3/8)^{1/2}$. Furthermore, if Ω_r is larger than N_∞, no growing disturbances radiate, which is just the condition of the frequency limit for evanescent waves.

Based on these arguments, means are examined by which IGW radiate into $\mathscr{R}_1$ from eddies below $\mathscr{R}_1$, which arise due to linear instability of a basic-state parallel flow. If the wavelength, frequency, and growth rate of the perturbation to the horizontal flow are such that the penetration condition $|\mathscr{D}| > 1$ is satisfied in $\mathscr{R}_1$, then IGW that radiate in this way are referred to hereafter as primary internal gravity waves. If the condition is not satisfied, however, IGW may nevertheless be generated by eddies that develop nonlinearly to a state such that the frequency and growth rate of the disturbances extending into $\mathscr{R}_1$ may satisfy the penetration condition. For example, Davis and Peltier (1979) suggested that vortex merging processes might effectively give rise to disturbances of longer wavelength and thereby lead to the emission of internal wave radiation into the far field of a shear layer. Also, Fritts (1984) and Chimonas and Grant (1984) have examined the possibility for "envelope radiation" by excitation of a propagating mode through resonant interaction of two growing modes in a resonant triad. Nei-
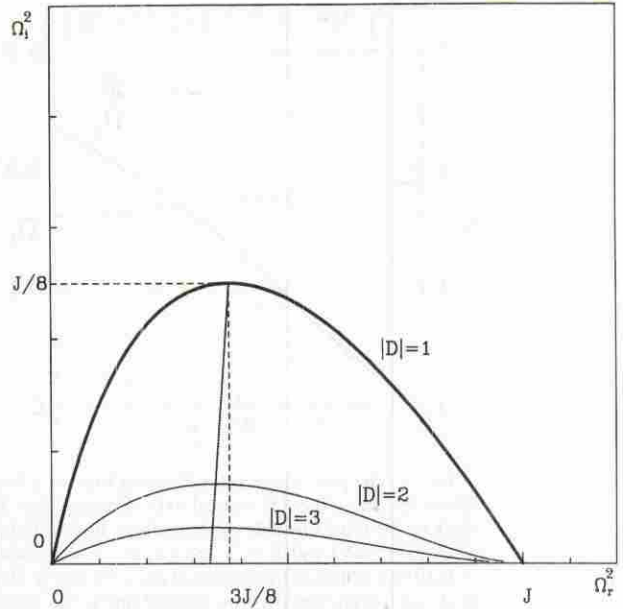

FIG. 2. Contours of the penetration ratio $|\mathscr{D}|$ as a function of the squared frequency and growth rate of a disturbance into a region of constant $N^2 = J$. The dark contour corresponds to $|\mathscr{D}| = 1$, which determines the fastest growth rate of the disturbance of a given frequency. The dotted line represents those values of Ω_r^2 for which the penetration ratio is greatest for disturbances of a given growth rate.

ther of these analyses recognized the importance of the $N^2(z)$ profile in enhancing the strength of the emission mechanism, and only weak excitation was obtained. In the simulations that follow we demonstrate a third nonlinear mechanism for wave radiation whereby waves subharmonic to eddies are excited even though large-scale vortices do not merge. Hereafter, IGW that radiate as a consequence of nonlinear interactions in an initially linearly unstable mean state are referred to as secondary internal gravity waves. Though many nonlinear mechanisms for propagating wave excitation, such as those mentioned above, have been proposed, we believe that the generation of intense primary IGW emission is demonstrated here for the first time.

3. Nonlinear simulations

Nonlinear simulations restricted to two spatial dimensions are performed for unstable jet and shear flows in variable N^2 fluid. The first set of simulations will focus on the so-called Bickley jet for which the vertical profile of horizontal velocity is given by $U(z) = \text{sech}^2(z)$. The linear stability of the Bickley jet in uniformly stratified fluid has been the subject of many studies (e.g., Hazel 1972; Sutherland and Peltier 1992) and the nonlinear evolution in two dimensions of the Bickley jet flow with both uniform and variable N^2 has recently been investigated by Sutherland and Peltier (1994). In the second set of simulations to be discussed
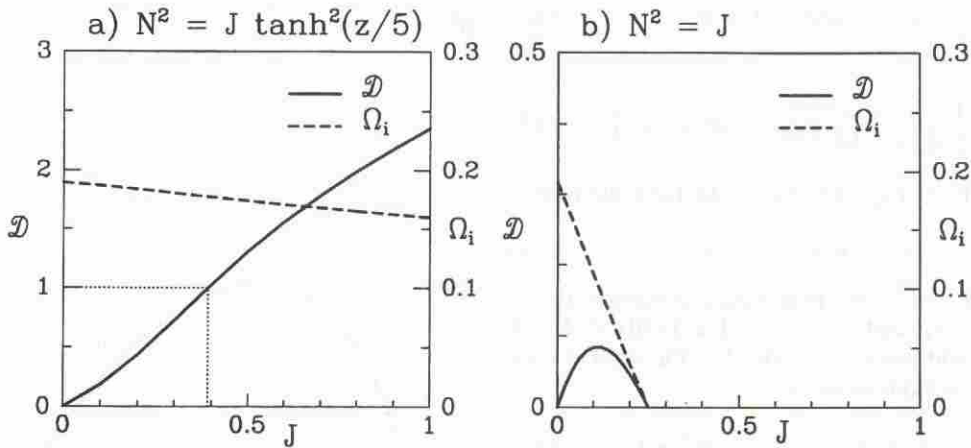
FIG. 3. The penetration ratio $\mathcal{D}$ (solid line) as a function of the bulk Richardson number J. Gradations of $\mathcal{D}$ are shown on the left vertical axis of both plates. The values are calculated for the structure on the upper flank of the most unstable mode of shear flow with horizontal velocity profile $U = \tanh(z)$ and with (a) $N^2 = J \tanh^2(z/R)$ and $R = 5$ and (b) $N^2 = J$ constant. In (a), the penetration condition is satisfied for $J > 0.391$ as indicated by the dotted lines, though in (b) the penetration condition is not satisfied for any value of J. Also represented by the dashed line is the growth rate Ω_i of the most unstable mode as a function of J. Gradations of Ω_i are shown on the right vertical axis of both plates.

herein, the evolution of a hyperbolic tangent shear layer (the so-called free mixing layer) will also be considered. The linear stability and two-dimensional nonlinear evolution of this flow in stratified fluid such that N^2 is large in the region of maximum shear has also been the subject of numerous studies (Hazel 1972; Pierrehumbert 1984; Klaassen and Peltier 1985; Smyth and Peltier 1989, 1993). The detailed nature of the internal wave critical layer in the hyperbolic tangent shear flow with constant N^2 has recently been considered by Lott and Teitelbaum (1992).

In simulations of the evolution of the Bickley jet in constant N^2 fluid (with N^2 nondimensionalized so that the flow is unstable for $N^2 < 0.127$), Sutherland and Peltier (1994) have shown that large-scale eddies are strained for N^2 as small as 0.005. Radiation of IGW was observed in simulations for $N^2 = 0.02$, although the eddies that developed in the simulation were strained to small scale so that forcing of IGW on the flanks of the jet was weak and the amplitude of the waves was small.

To allow for the development of large-scale eddies, N^2 is required to be small over a vertical range including the inflection points in the horizontal flow. In order to support the radiation of IGW in a broad frequency range, however, N^2 is required to be large on either flank of the jet. Therefore, a suitable profile for the square of the Brunt–Väisälä frequency that satisfies these criteria is given by Eq. (1): $N^2(z) = J \tanh^2(z/R)$. Here J is the bulk Richardson number, equal to the value of N^2 in the far field, and R is an adjustable length scale. Qualitatively, a background density distribution that gives rise to an N^2 profile of this form may occur as a consequence of mixing processes. Because large-

scale vertical motion is inhibited in the region of enhanced N^2, eddies that develop in the region of strong shear are confined to a waveguide whose vertical extent is determined by R. The background profiles of $U(z)$ and $N^2(z)$ for these archetypal flows are presented in Fig. 1. Tests of the robustness of the simulations in terms of the ability of these initial states to generate IGW of significant amplitude have been carried out for $0.01 < J < 1$ and for $1 < R < 10$.

Linear stability analysis applied to these background profiles also provides a useful theoretical framework in which to compare the predicted characteristics of growing disturbances that do propagate into a region of constant N^2 and U. Specifically, because N^2 is depressed in the region of large velocity variation, provided R is sufficiently large, the growth rate of the most unstable mode should not vary significantly over a large range of J in comparison with the penetration ratio $\mathcal{D}$. We examine this hypothesis in detail for shear flow with mean horizontal velocity $U(z) = \tanh(z)$ and, in case (a), $N^2 = J \tanh^2(z/5)$, and, in case (b), $N^2 = J$ (constant). In case (a), for J ranging from 0 to 1, we calculate the growth rate of the most unstable mode and the corresponding penetration ratio in the far field on the upper flank of the shear. These quantities are shown in Fig. 3a. Over the range of J shown, the growth rate decreases slightly and monotonically from 0.19 to 0.16 and therefore, according to Eq. (8), the estimate for the penetration depth of the disturbance increases only moderately, implying no significant radiation into the far field. In contrast, the penetration ratio increases from $\mathcal{D} = 0$, in which case disturbances are strongly trapped, to $\mathcal{D} \approx 2.35$, in which case primary IGW are generated. In case (b), for J ranging from 0 to 0.25,

$\mathscr{D}$ and Ω_i are calculated for the most unstable mode as in case (a). These quantities are shown in Fig. 3b. In this case, the growth rate decreases from 0.19 to 0, which, according to Eq. (8), corresponds to an infinite increase in penetration depth. Nonetheless, it is well known from simulations of shear flow in constant N^2 fluid (e.g., Smyth and Peltier 1989) that no significant generation of IGW occurs in this case, and so the penetration depth is an inappropriate measure of the ability for the flow to radiate. Over the same range of J in this case, however, $\mathscr{D}$ is much smaller than 1 and so the penetration condition is not satisfied for any J, a result consistent with observations. This example clearly illustrates the usefulness of the penetration ratio that we have defined in providing a prognostic assessment of the effectiveness of a linear instability as an IGW radiator.

The numerical model to be employed for the nonlinear simulations to be discussed in what follows is based on the methodology developed by Smyth and Peltier (1989) for the study of the evolution of Kelvin–Helmholtz and Holmboe waves. The evolution of the flow in two spatial dimensions is represented using the primitive equations for incompressible, Boussinesq fluid in a horizontally periodic channel with free-slip upper and lower boundary conditions. The nondimensional form of the fully nonlinear equations, in two spatial dimensions, for momentum conservation and for the conservation of internal energy are, respectively,

$$\frac{Du}{Dt} = -p_x' + \frac{1}{\text{Re}} \nabla^2 u \qquad (16)$$

$$\frac{Dw}{Dt} = -p_z' - J\rho' + \frac{1}{\text{Re}} \nabla^2 w \qquad (17)$$

and

$$\frac{D\rho'}{Dt} = \frac{N^2}{J} w + \frac{1}{\text{Re Pr}} \nabla^2 \rho', \qquad (18)$$

in which $D/Dt = \partial/\partial t + \mathbf{u} \cdot \nabla$ is the material derivative. The Reynolds number is $\text{Re} = \mathscr{U}\mathscr{L}/\nu$, in which $\mathscr{U}$ is the maximum velocity of the initial state background flow, $\mathscr{L}$ is a characteristic measure of the jet width or shear layer depth, and ν is the kinematic viscosity. The Prandtl number is $\text{Pr} = \nu/\kappa$ in which κ is the thermal diffusivity. The pressure fluctuation p' is the total pressure less the pressure $\bar{p}(z)$ that is in hydrostatic balance with the background density $\bar{\rho}(z)$.

For the purpose of numerical integration of (16)–(18), it is convenient to evolve the flow using the vorticity–streamfunction representation since the model then reduces to the evolution equations for two coupled fields, namely, ω and ρ'. The vorticity equation that follows from Eqs. (16) and (17) is

$$\frac{D\omega}{Dt} = J\rho_x' + \frac{1}{\text{Re}} \nabla^2 \omega, \qquad (19)$$

in which $\omega = u_z - w_x$ is the spanwise component of vorticity. The components of the velocity vector may be calculated from the streamfunction, which is itself found by inverting the elliptic differential equation:

$$\nabla^2 \psi = -\omega. \qquad (20)$$

Diffusion in the model is enhanced at small scales to a degree that is determined by the Reynolds number and the Prandtl number. The simulations to be described here are performed with a moderately high Reynolds number, $\text{Re} = 600$, and with $\text{Pr} = 1$. Vertical motion is damped near the upper and lower boundaries of the channel by inserting a "sponge" layer in which the kinematic viscosity is gradually enhanced. Specifically, over the top and bottom 15% of the domain, Re is taken to decrease linearly from its middomain value to 1 at the boundaries. The inclusion of such damping into the model is sufficient to eliminate the reflection of small amplitude disturbances. Simulations are advanced in time only until vertically propagating waves of nonnegligible amplitude are incident on the damping region.

The most unstable mode of linear theory for the initial state background flow is determined through the application of a Galerkin stability analysis employing finite Re and Pr (e.g., Klaassen and Peltier 1985). This analysis is performed on domains of sufficient spatial scale and high resolution that the predicted growth rate is relatively insensitive to any further increase in either of these quantities. The most unstable mode, which is normalized so that the maximum vertical velocity of the perturbation is initially set to be $0.05\mathscr{U}$, is superposed on the background fields of density and horizontal velocity, and a small amplitude random component is added across the wavenumber spectrum. To ensure that the growth rate σ predicted by linear theory is adequately reproduced, the predicted growth rate is compared to the initial growth rate σ_0 of the perturbation determined in simulations by examination of the initial change in perturbation energy E'. Specifically, σ is compared with $\sigma_0 = \frac{1}{2}E'(dE'/dt)$ and, in practice, agreement is generally found to within 5%.

In order to solve the model equations, the fields ω and ρ' are decomposed into horizontal spectral components and vertical derivatives are represented using a second-order accurate centered finite-difference scheme. Time stepping is achieved through application of the second-order accurate leapfrog scheme with an Euler backstep taken at regular intervals to eliminate splitting errors. To ensure that the results are not sensitive to resolution, simulations were performed for channels of varying width and the model equations were integrated with varying spatial and temporal resolution. The horizontal and vertical extents of the channel are assumed to have the nondimensional scales L_x and L_z, respectively. The centerline of the jet and the inflection point of the shear flow are each set to correspond with the midpoint of the channel.

In the simulations for which results will be reported below, the horizontal extent of the channel was adjusted to allow the growth of two wavelengths of the most unstable mode of linear theory so that subharmonic pairing of the finite-amplitude form of the most unstable mode is not precluded a priori. In the discussion that follows, a disturbance that propagates with the same horizontal wavenumber as the most unstable mode is said to be associated with a mode of wavenumber 2. Similarly, a subharmonic disturbance with horizontal wavelength twice that of the most unstable mode is said to be associated with a mode of wavenumber 1.

a. An overview of the simulations

Though we have found IGW to be generated in simulations of jet and shear flow with the above described initial conditions for a large range of the parameters J and R, the waves are excited through different mechanisms. To examine in detail the ways in which IGW develop and propagate, four specific cases are analyzed below. The characteristics and results of those simulations are summarized briefly in Table 1. In two cases, the evolution of jet flow is studied for moderate and large bulk Richardson number. Here J is sufficiently small in the first case that the penetration condition is not satisfied and J is sufficiently large in the second case that the penetration condition is satisfied. Similarly, in two studies of the evolution of shear flow, J is sufficiently small (large) that the penetration is not satisfied (is satisfied).

In the case we shall refer to as J1, simulations of jet flow are performed for the choice of parameters $J = 0.1$ and $R = 3$. Table 1 shows that $|\mathscr{D}| < 1$ on the

upper flank for the most unstable mode (and similarly $|\mathscr{D}| < 1$ on the bottom flank) and so the penetration condition predicts that the radiation of neutrally propagating IGW, if it occurs, must be a nonlinear process. We also note here that the PSC in this case is not satisfied and so waves of the same frequency as the growing normal mode are evanescent in the far field. In Fig. 4, the vorticity (panels a and b) and perturbation density (panels c and d) fields are shown at times $t = 100$ and 200 during the simulation. The vorticity fields are displayed over the vertical range $-5 \leqslant z \leqslant 5$ in order to better reveal the detailed structure of the eddies in the region of the flow with enhanced shear, and the zero contour is shown in bold to reveal the emission of IGW from eddies in the mean flow that are confined to the waveguide where N^2 is small. At time $t = 100$ the large-scale eddies maintain a horizontally periodic symmetry, though this symmetry is broken somewhat at $t = 200$. The perturbation density fields are shown over the full vertical extent of the domain, including the damping regions near the boundaries that extend from $-40 \leqslant z \leqslant -28$ and $28 \leqslant z \leqslant 40$. The figure demonstrates that IGW persist and propagate upward even when eddies evolve into small-scale structures through wave–mean flow interaction. At $t = 200$, IGW of wavenumber 2 are observed to have propagated upward and downward, the two wave packets being centered about $z \approx \pm 20$. Though the flow does radiate waves, a fact which seems to contradict the predictions of the penetration condition, the disturbance is not evanescent in the far field and must therefore be associated with a frequency different from that of the most unstable mode. We conclude that the generation of these waves involves a nonlinear mechanism and the waves them-

TABLE 1. A brief summary of the results of four nonlinear simulations. The most unstable mode characteristics are given with respect to a stationary frame of reference; $\mathscr{D}$ is the penetration ratio.

Simulation label and flow parameters	Most unstable mode characteristics ($z \gg 0$)	Comments
J1: Jet flow $J = 0.1$	$\alpha = 0.95$ $\omega_r = 0.430$ $\omega_i = 0.150$ $\mathscr{D} = -0.20$	PSC and penetration condition are not satisfied weak radiation of wavenumber 2 APE $\gg$ KE in far field
S1: Shear flow $J = 0.1$ $R = 3$	$\alpha = 0.49$ $\omega_r = 0.0$ $\omega_i = 0.180$ $\mathscr{D} = 0.16$	PSC and penetration condition are not satisfied radiation primarily of wavenumber 1 APE $\gg$ KE in far field
J2: Jet flow $J = 1.0$ $R = 5$	$\alpha = 1.13$ $\omega_r = 0.609$ $\omega_i = 0.130$ $\mathscr{D} = -2.92$	PSC and penetration condition are satisfied radiation of wavenumber 2 APE $\approx$ KE in far field
S2: Shear flow $J = 1.0$ $R = 5$	$\alpha = 0.61$ $\omega_r = 0.0$ $\omega_i = 0.160$ $\mathscr{D} = 2.35$	PSC and penetration condition are satisfied strong radiation of wavenumber 2 APE $\approx$ KE in far field

a) J1, t=100.0: ω   b) J1, t=200.0: ω
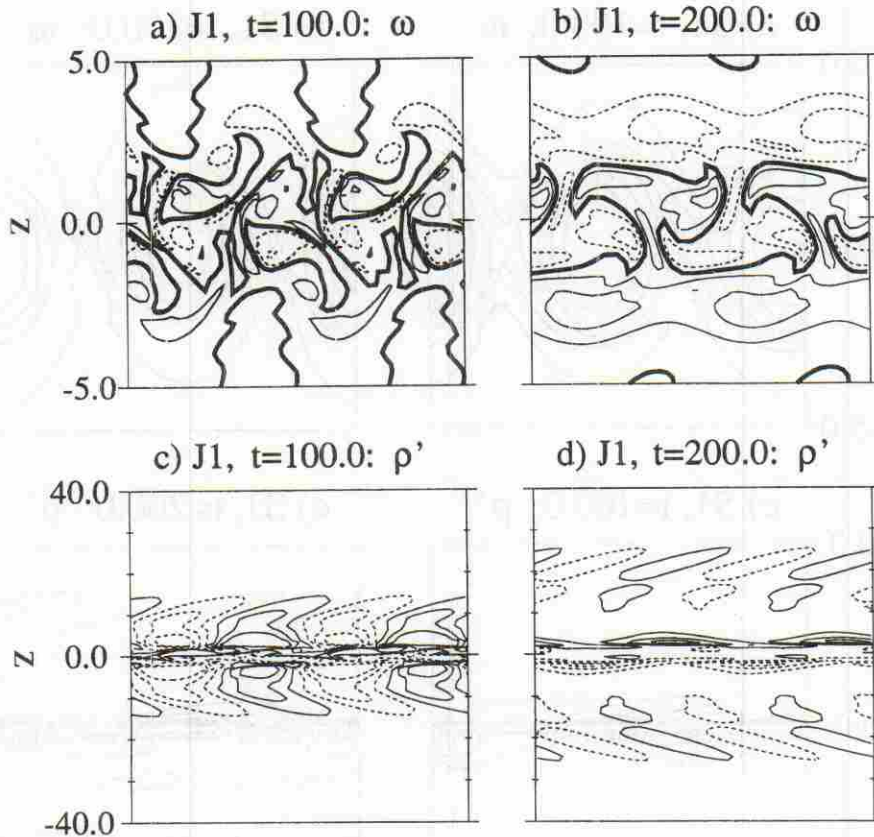
c) J1, t=100.0: ρ'   d) J1, t=200.0: ρ'

FIG. 4. Vorticity fields of jet flow for $J = 0.1$ and $R = 3$ at times (a) $t = 100$ and (b) 200 shown for $-5 < z < 5$. The horizontal extent of the computational domain is twice the wavelength of the most unstable mode of linear theory. In (a), contours are set at 0 and ±0.4. In (b), contours are set at 0, ±0.1, and ±0.2. Positive (negative) contours are solid (dashed) curves and the zero contour is shown in bold to enhance the details of the IGW radiation. Even at late times, pairing is inhibited between large-scale vortices of like sign. Fluctuation density fields are shown at times (c) $t = 100$ and (d) 200 over the full vertical extent of the domain. Contours are set at ±0.05, ±0.15, and ±0.25 in both plates. Positive (negative) contours are solid (dashed) curves. These plates show wave radiation from the top and bottom flank of the jet with downstream phase tilt.

selves must be secondary IGW according to the previous discussion.

As in case J1, in S1 the evolution of the hyperbolic tangent shear layer is studied for parameters $J = 0.1$ and $R = 3$. For this case, the penetration condition is not satisfied, and so we predict that the radiation of waves may occur only due to nonlinear interactions. The vorticity and perturbation density fields from simulations for S1 are shown in Fig. 5 at times $t = 100$ and 200. Panels (a) and (b) show the vorticity field over the vertical range $-5 \leq z \leq 5$, and panels (c) and (d) show the perturbation density field over the full vertical extent of the channel $-80 \leq z \leq 80$, including the boundary damping region that extends from $-80 \leq z \leq -56$ and $56 \leq z \leq 80$. At time $t = 100$, the propagation of a wavenumber 2 disturbance into the more strongly stratified fluid on either flank of the shear layer is suppressed. At time $t = 200$, however, a secondary wave of horizontal wavenumber 1 develops

from the eddies of wavenumber 2 on either side of the shear layer. The IGW are not retarded in this case and rapidly propagate vertically away from the shear layer. In comparison with IGW that radiate from the jet, the backward tilt of the phase lines of IGW that radiate above the shear at $t = 200$ is in accordance with the upstream phase speed of waves with respect to the background flow. This simulation demonstrates a novel nonlinear mechanism whereby IGW may be generated in a stratified, parallel flow. The mechanism is similar to that suggested by Davis and Peltier (1979), who proposed that IGW may be generated by a vortex pairing process. In this simulation, however, large-scale eddies near the critical layer do not entirely merge during the emission process. The IGW appear to be generated through subharmonic excitation by large-scale, horizontally periodic eddies. Consistent with the predictions of the penetration condition, waves excited in this manner are secondary IGW.
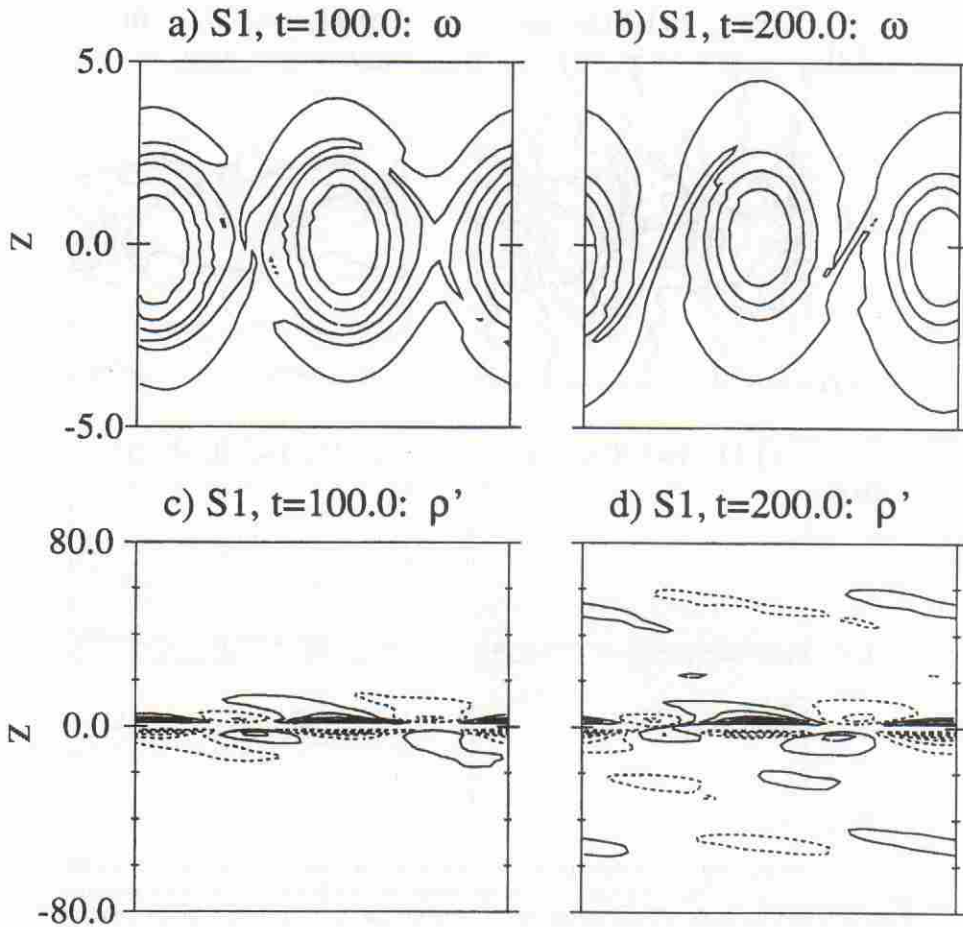
FIG. 5. Vorticity fields of shear flow for $J = 0.1$ and $R = 3$ at times (a) $t = 100$ and (b) 200 shown for $-5 < z < 5$. The horizontal extent of the computational domain is twice the wavelength of the most unstable mode of linear theory. Contours are set at 0.1, 0.3, 0.5, 0.7, and 0.9 in both plates. Fluctuation density fields are shown at times (c) $t = 100$ and (d) 200 over the full vertical extent of the domain. Contours are set at ± 0.1, ± 0.3, ± 0.5, and ± 0.7 in both plates. Positive (negative) contours are solid (dashed) curves. At $t = 100$, the development of waves that radiate with horizontal wavenumber 1 and retrograde phase tilt is apparent at this time even though the eddy energy is resolved primarily in the wavenumber 2 mode. At $t = 200$, a wave packet of horizontal wavenumber 1 propagates vertically away from the mixing region although the large-scale vortices in this region have not merged.

If the bulk Richardson number is larger on the flanks of the jet or shear layer, then the penetration condition $|\mathscr{D}| > 1$, where $\mathscr{D}$ is given by Eqs. (12) and (13), can be satisfied by a larger class of IGW and, in particular, primary generation of IGW may be more likely to occur. This hypothesis is investigated by performing simulations for the choice of parameters $J = 1$ and $R = 5$ for both jet flow (case J2) and shear flow (case S2). The bulk Richardson number is such that waves of frequency less than unity may radiate into the far field. In both cases, therefore, the frequency of the most unstable mode with respect to the asymptotic flow is well within the limit for propagating waves. Furthermore, the growth rate of the most unstable mode is such that the penetration condition is satisfied in both cases,

and therefore the primary generation of IGW is expected to occur.

The vorticity and perturbation density fields at times $t = 50$ and 100 for J2 are shown in Fig. 6. The vertical extent of the domain ranges from $-5 \leq z \leq 5$ for the vorticity fields, and the domain of the perturbation density fields is shown ranging from $-40 \leq z \leq 40$. The outward propagation of IGW with large vertical wavenumber radiating from large-scale vortex centers is apparent in this case from the zero contour shown in bold in panels (a) and (b). The waves persist and propagate outward even when the vortex cores weaken significantly at time $t = 100$. We have found that the phase speed of the waves in the far field corresponds with that of the initial mode of instability, which supports
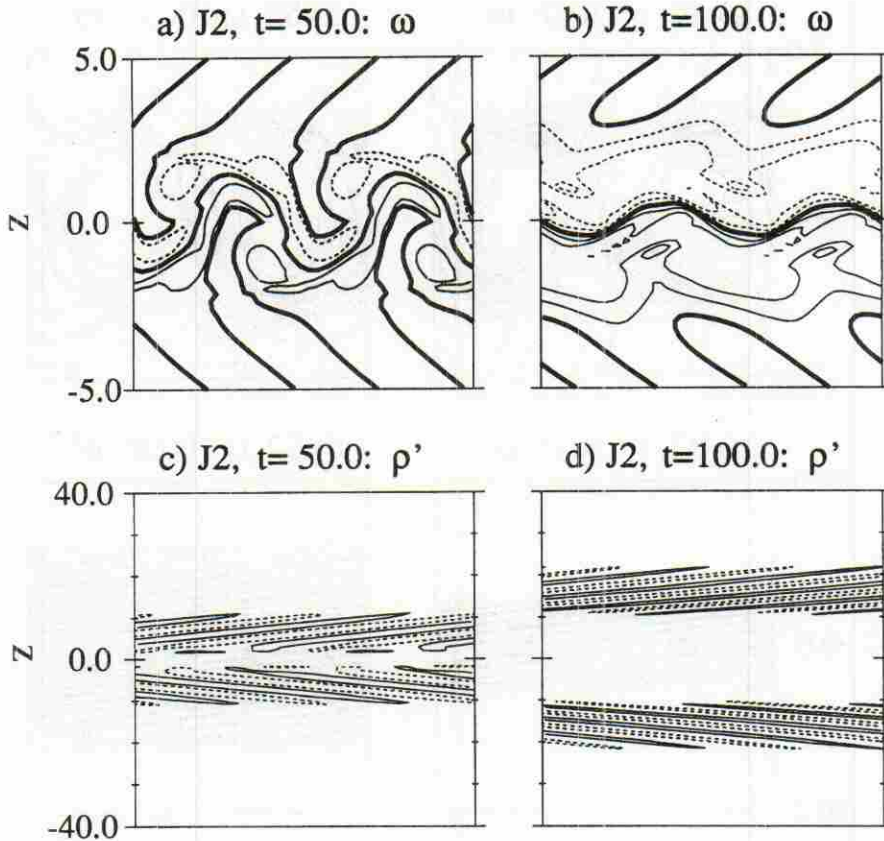
a) J2, t= 50.0: ω   b) J2, t=100.0: ω

c) J2, t= 50.0: ρ'   d) J2, t=100.0: ρ'

FIG. 6. Vorticity fields of jet flow for $J = 1.0$ and $R = 5$ at times (a) $t = 50$ and (b) 100 shown for $-5 \leqslant z \leqslant 5$. The horizontal extent of the computational domain is twice the wavelength of the most unstable mode of linear theory. In (a), contours are set at 0 and ± 0.5. In (b), contours are set at 0, ± 0.1, and ± 0.2. Positive (negative) contours are solid (dashed) curves, and the zero contour is shown in bold to enhance the details of the IGW radiation. Fluctuation density fields are shown at times (c) $t = 50$ and (d) 100 over the full vertical extent of the domain. Contours are set at 0.05 (solid curve) and -0.05 (dashed curve) in both panels. These panels show wave radiation from the top and bottom flank of the jet with downstream phase tilt. The intensity of wave radiation from the mixing region appears to reduce at later times as the flow stabilizes. Nonetheless, waves continue to propagate outward even when the vortices in the central region of the jet weaken.

the prediction of the penetration condition that the disturbance in the far field is composed of primary IGW.

Similarly, the vorticity and perturbation density fields at times $t = 50$ and 100 for S2 are shown in Fig. 7. The figure demonstrates strong and continuous wave radiation, although it is apparent in panels (a) and (b) that the entrainment of fluid into the mixing region gives rise to strong baroclinic torques.

In all four simulations, though the nature of the radiating wave field may be quite different near $|z| = R$ at later times, a study of the vertical profiles of Reynolds stress, KE, and APE in section 3c demonstrates that the waves that radiate in the far field propagate outward and are unlikely to be affected by subsequent nonlinear developments in the mixing region.

b. *Diagnostic analyses of the characteristics of the emitted waves*

At fixed times in each of the simulations we have examined, the horizontally averaged wave kinetic energy (KE) and available potential energy (APE) are calculated. These are defined, respectively, by

$$\langle \text{KE} \rangle_x = \frac{1}{2} \langle u'^2 + w'^2 \rangle_x \qquad (21)$$

and

$$\langle \text{APE} \rangle_x = \frac{1}{2} \left\langle \frac{J^2}{N^2} \rho'^2 \right\rangle_x, \qquad (22)$$

in which $w' = w$ is the vertical velocity field and $u' = u - \langle u \rangle_x$ is the horizontal velocity of waves super-
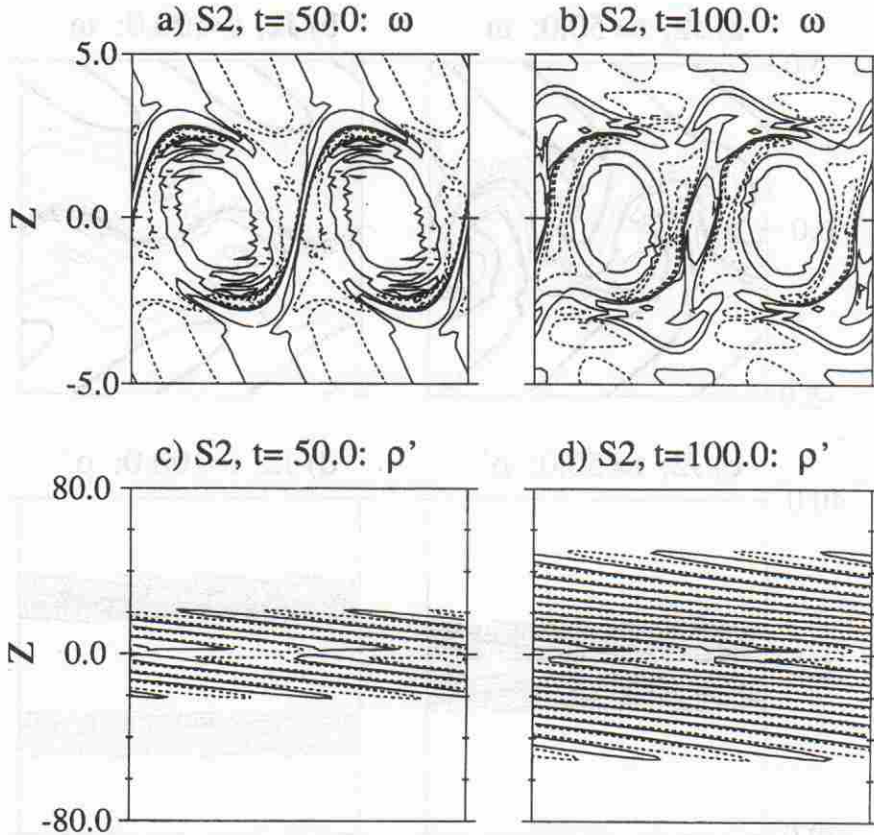
FIG. 7. Vorticity fields of shear flow for $J = 1.0$ and $R = 5$ at times (a) $t = 50$ and (b) 100 shown for $-5 < z < 5$. The horizontal extent of the computational domain is twice the wavelength of the most unstable mode of linear theory. Contours are set at ± 0.2 and ± 0.6 in both plates. Positive (negative) contours are solid (dashed) curves. Fluctuation density fields are shown at times (c) $t = 50$ and (d) 100 over the full vertical extent of the domain. Contours are set at 0.1 (solid curves) and -0.1 (dashed curves) in both plates. Though the eddies in the mixing region are not well resolved, simulations at double resolution also reproduce the strong and continuous emission of IGW that emanate from the mixing region for the times shown.

posed on the background (horizontally averaged) flow. The above expression for wave APE is exact only in regions of the fluid in which N^2 is constant. Since the primary interest of this study concerns the energetics of waves that exist in the region of enhanced $N^2 \approx J$ in the far field, Eq. (22) together with (21) can be taken to be an accurate measure of the energy of the IGW. For plane IGW in nonrotational, inviscid fluid with constant N^2, it is well known that energy is equipartitioned over the KE and APE forms (e.g., Gill 1982, section 7.8). The Reynolds number is sufficiently large in simulations presented here that the analysis of the energetics of radiating disturbances may reasonably be compared with the energetics of plane IGW in inviscid fluid. This provides a useful characterization of the waves observed in the far field at late times in each case study.

The vertical transport of momentum is characterized by the horizontal average of the Reynolds stress

$$\tau = \langle u'w' \rangle_x = \sum_{n \geq 1} \langle u_n w_n \rangle_x, \tag{23}$$

which is the sum of contributions to the vertical transport by waves of horizontal wavenumber n. More accurately, at each time t the vertical flux of horizontal pseudomomentum $\mathscr{F}_M(z; t)$ may be calculated according to the formulas given by Shepherd (1990). However, in the far field (and in particular for $|z| \geq 10$) negligible differences were found between τ and $\mathscr{F}_M$ throughout all four simulations, a consequence of the fact that the vertical shear of the horizontal mean flow vanishes.

By symmetry, the total momentum conceivably available for upward vertical transport across a fixed level $z = z_0 > 0$ from the initial basic state is given by

$$M_T = \int_0^{z_0} \bar{U}(z) dz. \tag{24}$$

With $z_0 = 10$, $M_T = 1.0$ for jet flow and $M_T = -9.3$ for shear flow. (In practice, the inflection points of the jet are situated at vertical levels where N^2 is finite and therefore the mean flow may become Richardson number stable after the flow evolves nonlinearly for some time. The total momentum available, which we have defined above for jet flow, in this sense overestimates the actual momentum that may be imparted to the radiating wave field). The pseudomomentum flux may be integrated in time to give the total vertical transport of horizontal pseudomomentum over the duration of each simulation. We define the ratio

$$\eta = \frac{1}{M_T} \int \mathcal{F}_M(z_0; t)\, dt \qquad (25)$$

as a reasonable measure of the efficiency of wave radiation.

c. Results of the diagnostic analyses

The results of these diagnostic analyses applied to the simulations described in section 3a are discussed in detail below. For purposes of an initial comparison, Table 2 summarizes some of the more relevant results for cases J1 and S1 at times $t = 100$ and 200, and for cases J2 and S2 at times $t = 50$ and 100. The table gives the horizontally averaged KE and APE evaluated at a vertical level z_m, which corresponds approximately to the center of the region of apparent wave propagation on the top flank of the jet/shear layer. Explicitly, the value of z_m is the greatest height at which the contribution to the Reynolds stress is a maximum. This height is generally coincident with the level at which the wave energy density is greatest. At late time in simulation S1, energy in wave APE form is greater than the wave KE. In simulations J1, J2, and S2, however, the peak values of wave KE and APE are comparable, which is a property characteristic of plane IGW, as previously mentioned. That the energy distribution of KE and APE is not equal in case S1 is an indication that the wave field is not composed of the superposition of neutrally propagating plane waves.

In order to measure the relative efficiency by which radiating waves transport momentum vertically from the source region in the mean flow, the mean vertical flux of horizontal pseudomomentum across a level $z_0 = 10$ is calculated throughout each simulation. The pseudomomentum flux as a function of time is shown for all four cases in Fig. 8. The figure shows that waves propagating upward from the jet (shear layer) carry forward (backward) momentum with respect to the mean flow at z_0 consistent with the tendency for waves to accelerate (decelerate) the background flow in the far field. In cases J1 and S1, pseudomomentum is carried across the vertical level $z = z_0$ in pulses and for late times must be associated with disturbances excited by eddies in the mixing region and not with the initial linearly unstable mode. In contrast, for the times shown

TABLE 2. KE and APE at z_m corresponding to the largest vertical level above $z = R$ at which the Reynolds stress is a maximum. For J2 and S2 at $t = 50$, KE and APE are evaluated at $z = R$ (where APE is well defined) although the maximum Reynolds stress occurs at $z = 4.7$ and $z = 0.0$, respectively. Otherwise, z_m is an approximate measure of the position of the center of the wave packet moving upward from the top flank of the jet or shear flow under consideration. The last column in the table is a measure of the vertical flux of horizontal pseudomomentum across the level $z_0 = 10$, which is time integrated from the start of the simulation of time t. The value is given as the ratio to the total momentum initially available in the basic state for upward transport (see text).

Simulation and time	z_m	KE (z_m)	APE (z_m)	η: Momentum transfer ratio across $z_0 = 10$
J1: $t = 100$	9.5	0.00088	0.00092	0.011
$t = 200$	14.7	0.00013	0.00014	0.018
S1: $t = 100$	27.5	0.00009	0.00004	0.001
$t = 200$	50.3	0.00034	0.00041	0.002
J2: $t = 50$	5.0	0.0044	0.0045	0.007
$t = 100$	16.4	0.0011	0.0011	0.085
S2: $t = 50$	5.0	0.0621	0.0579	0.045
$t = 100$	14.7	0.0534	0.0538	0.340

in cases J2 and S2, waves carry pseudomomentum across z_0 in a single smooth pulse. The integral of the pseudomomentum flux in time is the total transfer of pseudomomentum across z_0; this value is compared with the total available momentum of the initial mean state between $z = 0$ and $z = z_0$ to give the efficiency η defined by Eq. (25).

The efficiency is given in the last column of Table 2. Comparing the two jet cases, the momentum transport appears to be moderately more efficient in case J2. On the other hand, though in case S1 wave radiation is weak, case S2 is extraordinarily efficient in extracting energy from the mean flow, transporting over one-third of initial horizontal momentum of the shear layer away from the mixing region. The transport of momentum by primary IGW is generally more efficient than transport by secondary IGW. In jet flow, however, the total momentum transport is limited by the nonzero flux of pseudomomentum away from the mixing region, a restriction which is not imposed by the spatial vertical symmetry of shear flow examined here. We demonstrate this symmetry explicitly in our study of the Reynolds stress profiles below.

For case J1 we show in Fig. 9 the vertical profiles of (a) mean horizontal velocity, (b) Reynolds stress, (c) KE, and (d) APE at time $t = 100$, and the vertical profiles of the same quantities (panels e–h, respectively) at time $t = 200$. The profile of APE is not shown for $|z| < R$, within which region the approximation APE $\approx \frac{1}{2}(J^2/N^2)(\rho')^2$ may not be valid. At both times shown, the jet is most intense for $|z| < R$ and is only weakly accelerated by the divergence of wave pseudomomentum flux in the far field. At $t = 100$, the ver-
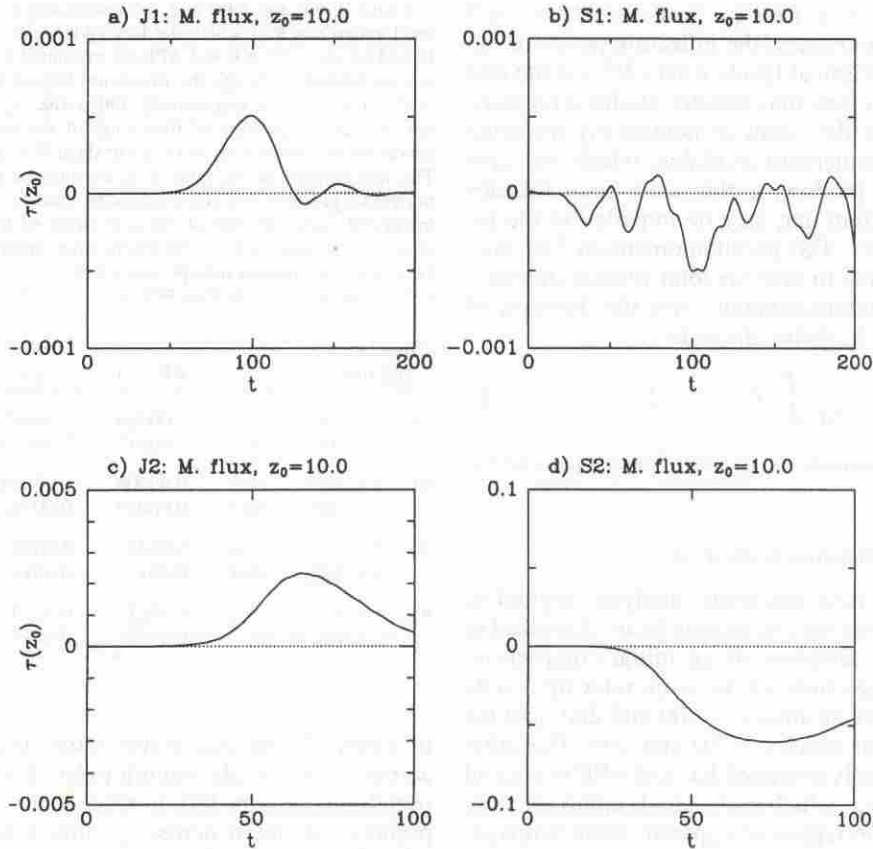
FIG. 8. The mean vertical flux of horizontal pseudomomentum across $z = 10$ is shown for cases (a) J1, (b) S1, (c) J2, and (d) S2 over the times of each simulation. The upward propagation of waves emanating from a jet flow tends to accelerate the background flow and carry positive forward momentum, whereas the waves emanating upward from a shear flow tend to decelerate the background flow and carry negative forward momentum. The flux of momentum is greatest in cases J2 and S2.

tical profiles of wave KE and wave APE demonstrate that the energy of the wave is in equipartition. At $t = 200$ the wave packets on either flank of the jet are separate from the jet core. That the energy is radiated away from the jet at both times is indicated by the sign of the Reynolds stress, which shows the upward transfer of forward momentum on the top flank of the jet and the downward transfer of forward momentum on the bottom flank. It is a consequence of the symmetry of the jet that the total momentum carried away from the mixing region by waves is positive. The vertical extent of the IGW wave packets, which may be adequately measured by the range over which the stress is of one sign on either flank of the jet, is larger at $t = 200$ than at $t = 100$, and the peak value of energy is smaller. These observations are attributed in part to wave dispersion.

In S1, as remarked earlier, waves that are excited by the most unstable mode and propagate vertically into the region of enhanced N^2 are expected to be evanescent. Figure 10, the panels of which correspond to those of Fig. 9, shows the results of the simulation analyses.

Like case J1, the vertical extent of the mixing region does not vary over the times shown, and the momentum flux divergence of propagating waves in the far field is small so that the mean flow is not significantly decelerated. Furthermore, at late times the energy associated with the waves is manifested primarily in the form of APE. At $t = 200$, the energy of waves on either flank of the shear layer is significantly greater and must result from a different generation mechanism for the radiation of waves. Though a fraction of this energy is carried by the wavenumber 2 mode, it is apparent in Fig. 5d that the dominant waves radiating from the shear layer are those of horizontal wavenumber 1. This is quantified by calculating the partition of the wave energy into modes of wavenumbers 1 and 2 at times $t = 100$ and 200, the vertical profiles of which are shown in Fig. 11. The vertical range $|z| < R (=3)$ is excluded from these plates. The total energy of the wavenumber 1 mode is represented by the solid curve, and the energy of the wavenumber 2 mode is represented by the dashed curve. The energy in both modes is weak at time
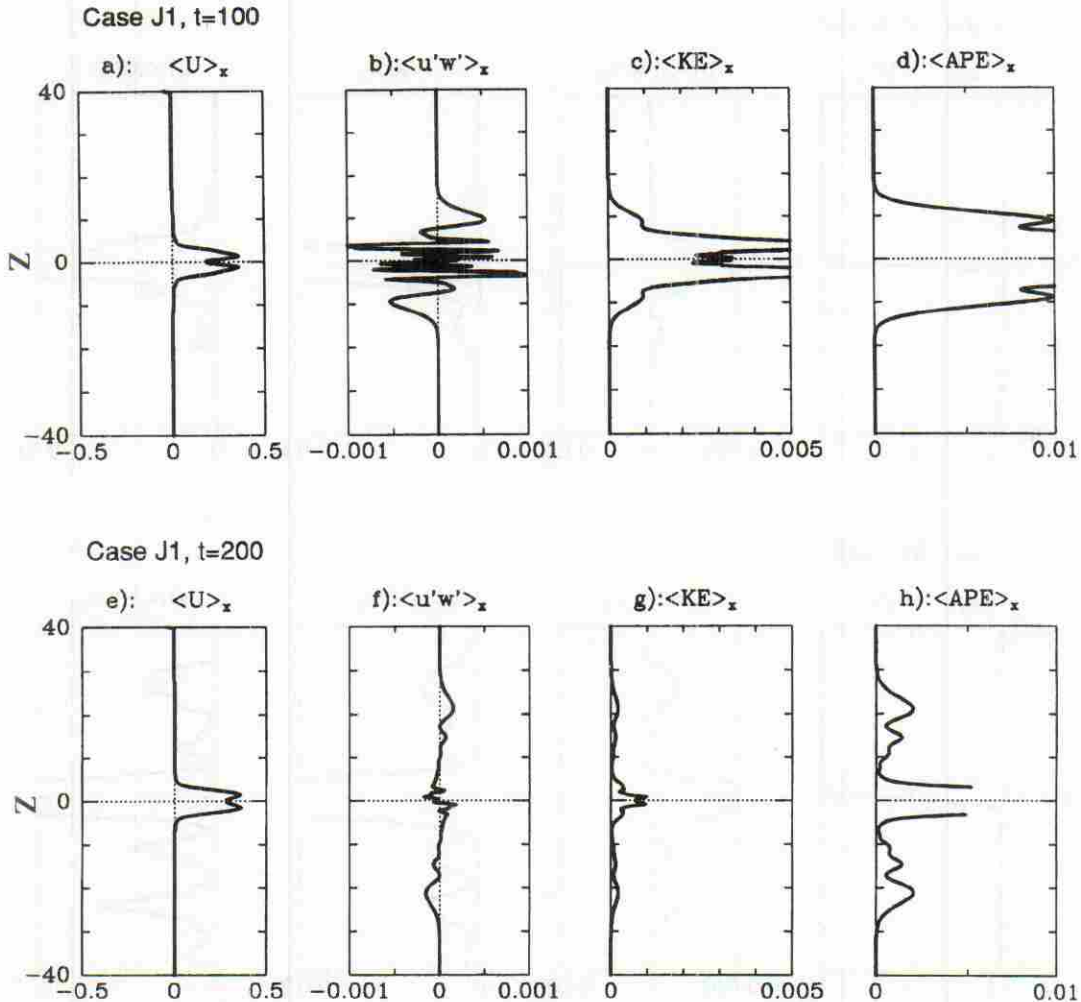
FIG. 9. From the jet simulation for $J = 0.1$ and $R = 3$ are shown vertical profiles at time $t = 100$ of (a) mean horizontal velocity, (b) Reynolds stress, (c) horizontally averaged wave kinetic energy, and (d) available potential energy. These four profiles are shown at time $t = 200$ in panels (e), (f), (g), and (h), respectively. The full vertical extent of the channel is shown in all eight panels and the horizontal scales are shown on each graph. APE is not shown for $|z| \leq R$ since this quantity may not be quadratic in ρ' over this range.

$t = 100$, though the wavenumber 2 mode is slightly more energetic on the flanks of the shear layer. At time $t = 200$, however, the energy in the wavenumber 1 mode is an order of magnitude larger than that in the wavenumber 2 mode on the flanks. Apparently, the energy transferred into the mode of wavenumber 1 is not due to a vortex pairing mechanism since the large-scale eddies shown in Fig. 5b have not merged to form a single larger eddy at this time. Rather, as the disturbance energy carried by the most unstable mode propagates upward, energy is transferred into the wavenumber 1 mode through subharmonic excitation by eddies. In Fig. 10 the vertical symmetry of the Reynolds stress, KE, and APE profiles is broken, which is a consequence of the sensitivity of the subharmonic excitation process to background noise.

In Fig. 12 the radiation of IGW is investigated at times $t = 50$ and 100 for the case J2. The panels correspond to those in Fig. 9. Like J1, the extent of the mixing region is confined within the waveguide $|z| < R$. Unlike J1, however, the wave KE is comparable to the APE, a feature characteristic of plane IGW. The significant broadening of the vertical energy and Reynolds stress distributions from $t = 50$ to $t = 100$ indicates the dispersive nature of the wave field on either flank of the jet. At $t = 100$, the wave KE is greatest in the wave packets on either flank of the jet. Although, in theory, the vertical group velocity for neutral plane waves is smaller in large N^2 fluid, in practice the vertical transport of energy is more efficient since waves penetrate more effectively into the strongly stratified medium.
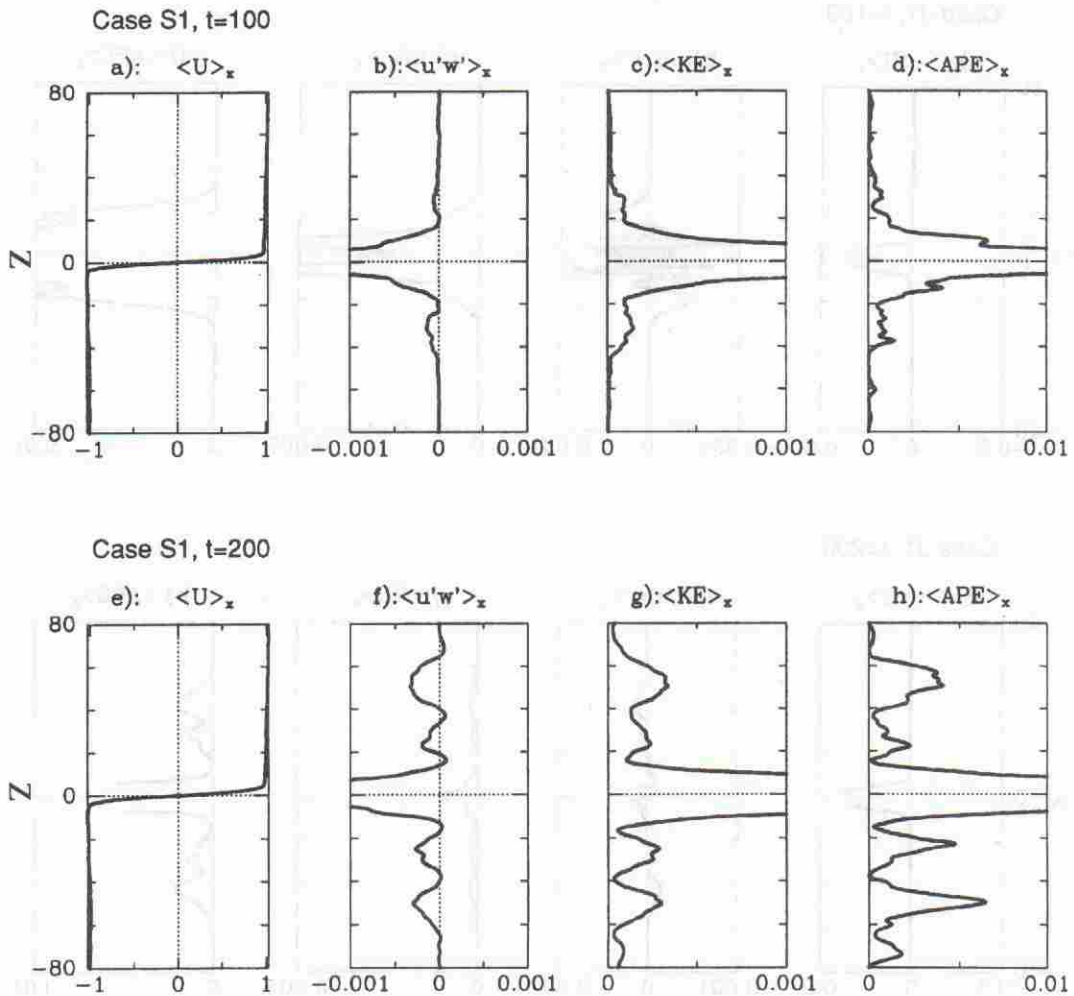
FIG. 10. From the shear simulation for $J = 0.1$ and $R = 3$ are shown vertical profiles at time $t = 100$ of (a) mean horizontal velocity, (b) Reynolds stress, (c) horizontally averaged wave kinetic energy, and (d) available potential energy. These four profiles are shown at time $t = 200$ in panels (e), (f), (g), and (h). The full vertical extent of the channel is shown in all eight panels, and the horizontal scales are shown on each graph. APE is not shown for $|z| \leq R$ since this quantity may not be quadratic in ρ' over this range.

The results of the simulation for S2 are shown in Fig. 13 at times $t = 50$ and 100. The panels correspond to those of Fig. 9. In this case the energy of the wave packet, equally distributed in the form of KE and APE, is more than an order of magnitude larger and more broadly distributed than the energy of the IGW in J2. Whereas the peak energy of the waves that radiate in J2 is significantly smaller at $t = 100$, there is only a small decrease in energy for waves that radiate in S2. The mean horizontal velocity profiles show that the waves propagating away from the shear layer act to decelerate (accelerate) the flow on the top (bottom) flank of the region of maximum shear. However, the maximum strength of the shear does not decrease significantly during the simulation. By symmetry, the vertical flux of horizontal pseudomomentum associated

with the wave field is zero throughout the IGW emission process. Therefore, unlike the jet for which the total vertical flux of horizontal pseudomomentum of radiated waves is nonzero, conservation of momentum does not limit wave radiation from a shear flow. Furthermore, as the shear layer does not stabilize during the emission process, the flow on either flank is a large reservoir from which waves may continuously extract energy.

4. Conclusions

On the basis on linear theory, limits have been derived for the growth rate that must be satisfied for disturbances incident on a stratified region ($\mathcal{R}_1$) characterized by constant N^2 above some level z_1 in order that the disturbance propagate in $\mathcal{R}_1$. A disturbance is said
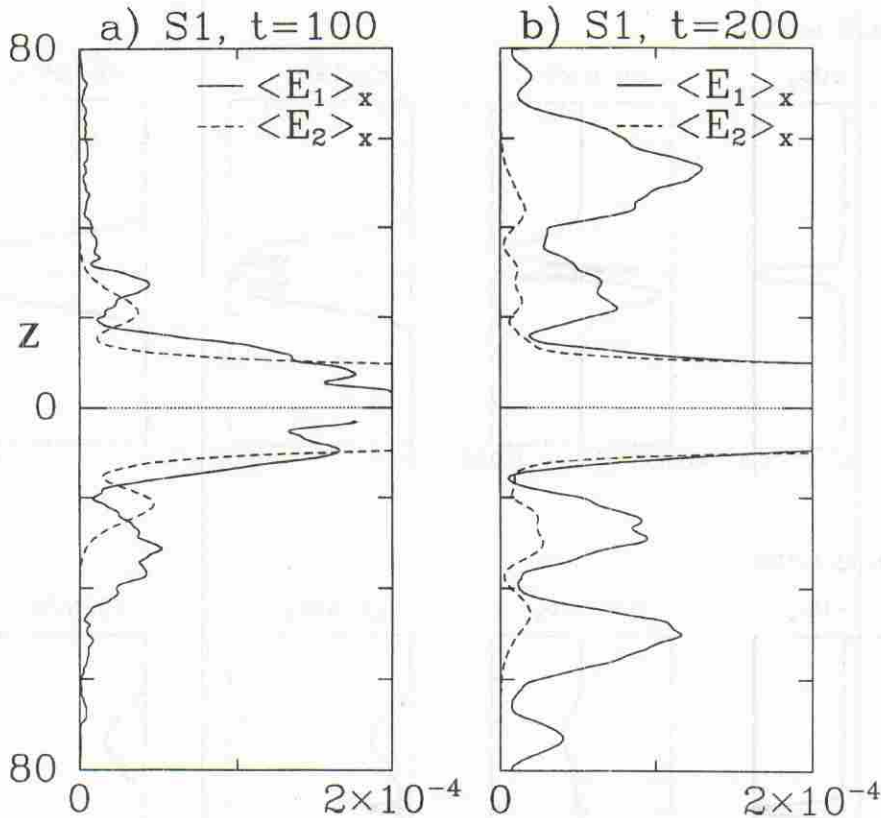
FIG. 11. The energy associated with modes of wavenumber 1 (solid curve) and wavenumber 2 (dashed curve) at time (a) $t = 100$ and (b) 200 for the case S1. These analyses demonstrate that energy is carried more effectively by IGW that radiate with twice the horizontal wavenumber of the most unstable mode of linear theory.

to propagate if a penetration condition, $|\mathscr{D}| > 1$, is satisfied, in which $\mathscr{D}$ is the ratio of the penetration depth to the vertical wavelength of the IGW excited by the incident disturbance. This condition restricts the growth rates of IGW that may propagate into $\mathscr{R}_1$ as a function of the Doppler-shifted frequency at which the waves are forced according to Eqs. (12) and (13). In particular, only waves with growth rate less than $N/8^{1/2}$ may successfully propagate into the far field. The same condition requires that waves penetrate into the far field only if the absolute value of the Doppler shifted frequency is less than N. This is precisely the evanescent condition that can be derived separately from the form of the dispersion relationship for plane IGW. Furthermore, in the case of growing disturbances in a uniform background flow, the penetration condition is a useful generalization of the phase speed condition given by McIntyre and Weissman (1978), which requires that the magnitude of the Doppler-shifted frequency be less than the Brunt–Väisälä frequency but does not explicitly pose restrictions to wave radiation in terms of the disturbance growth rate.

The predictions of this new penetration condition have been tested in simulations restricted to two spatial dimensions for both stratified jet and shear flow with $N^2 = J \tanh^2(z/R)$. In each case waves of significant amplitude are excited by eddies that develop in the mixing region, $|z| < R$. Phase lines of waves that radiate from a jet (shear) flow tilt in a downstream (upstream) direction, a characteristic consistent with IGW of positive (negative) horizontal phase speed with respect to the background horizontal wind speed. In case J1, for which $|\mathscr{D}| < 1$, waves are generated by a nonlinear mechanism. In J2 as well as J1, for which $|\mathscr{D}| > 1$, the energy density is equally in the form of KE and APE, consistent with the energy distribution characteristic of plane IGW. The total energy density of the waves in both cases is of the same order of magnitude. In case J2, though waves may be expected to extract momentum from the mean flow more efficiently, we demonstrate that the total upward flux in time of horizontal pseudomomentum is only moderately larger than in case J1 because the total pseudomomentum flux outside the mixing region is finite in both cases. The
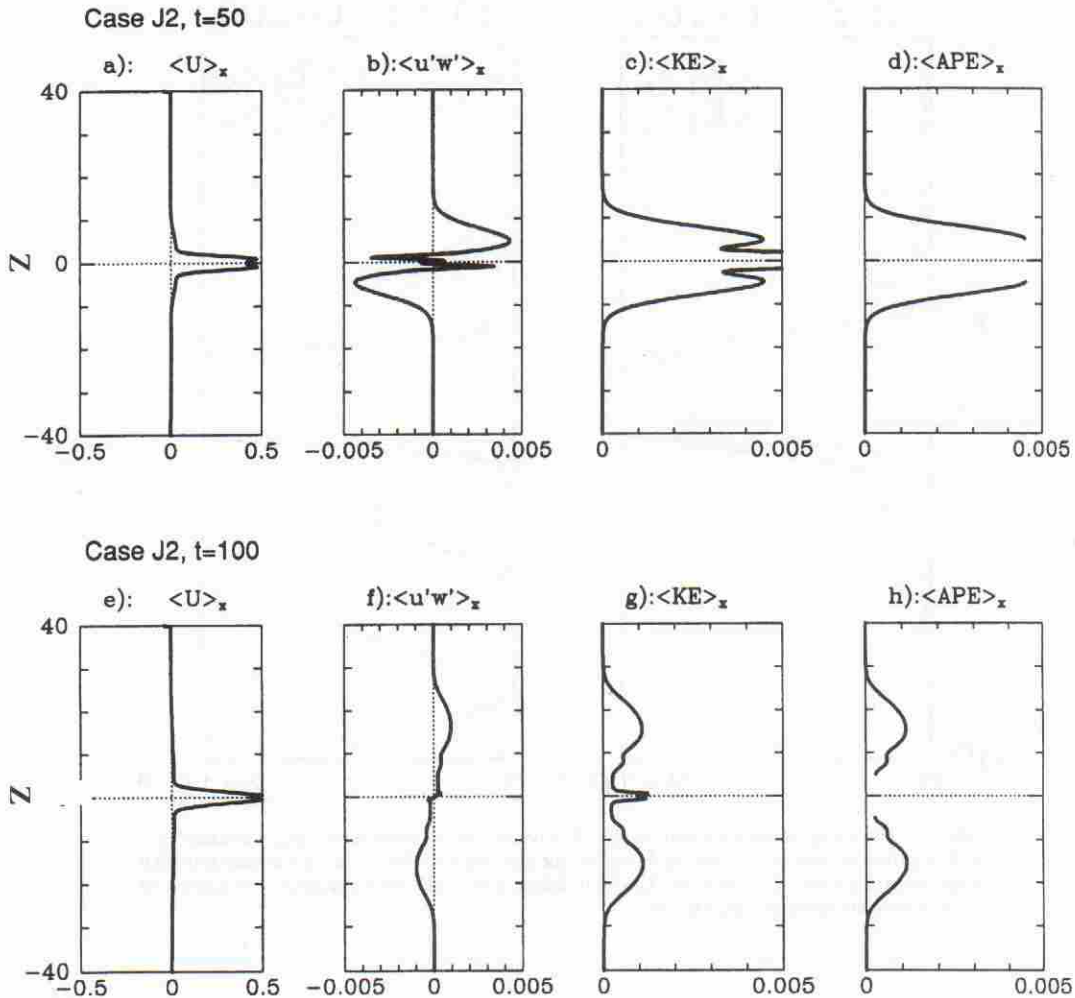
FIG. 12. From the jet simulation for $J = 1.0$ and $R = 5$ are shown vertical profiles at time $t = 50$ of (a) mean horizontal velocity, (b) Reynolds stress, (c) horizontally averaged wave kinetic energy, and (d) available potential energy. These four profiles are shown at time $t = 100$ in plates (e), (f), (g), and (h). The full vertical extent of the channel is shown in all eight plates and the horizontal scales are shown on each graph. APE is not shown for $|z| \leqslant R$ since this quantity may not be quadratic in ρ' over this range.

wave emission process, therefore, exerts an effective drag on the mean flow (radiation reaction), which, in turn, stabilizes and terminates further radiation.

In simulations of case S1, for which $|\mathscr{D}| < 1$, the Doppler-shifted frequency of the most unstable mode is greater than the frequency of the natural buoyancy oscillations. Disturbances with the same horizontal wavenumber as this mode are suppressed, though at later times in the simulation waves develop on the flanks of the shear layer with twice the horizontal wavelength of the most unstable mode of linear theory. This subharmonic excitation occurs though large-scale vortices in the mixing region have not merged and represents a novel nonlinear generation mechanism of IGW. The wave APE in the far field is greater than the wave KE. In case S2, however, for which

$|\mathscr{D}| > 1$, the energy of radiated waves is distributed approximately equally between the KE and APE forms. Of the four cases considered here, this last simulation, in particular, demonstrates the efficiency of the mechanism through which momentum is transported vertically away from the unstable region when the region has a Brunt–Väisälä frequency that is significantly lower from that of the surrounding fluid.

Our contention is that the internal wave emission mechanisms discovered in the analyses reported here are liable to be extremely important to understanding the origins of a significant fraction of the internal wave activity observed in the middle atmosphere, for which a source in parallel shear instability has often been postulated in the past but for which no efficient mechanism has been previously identified.
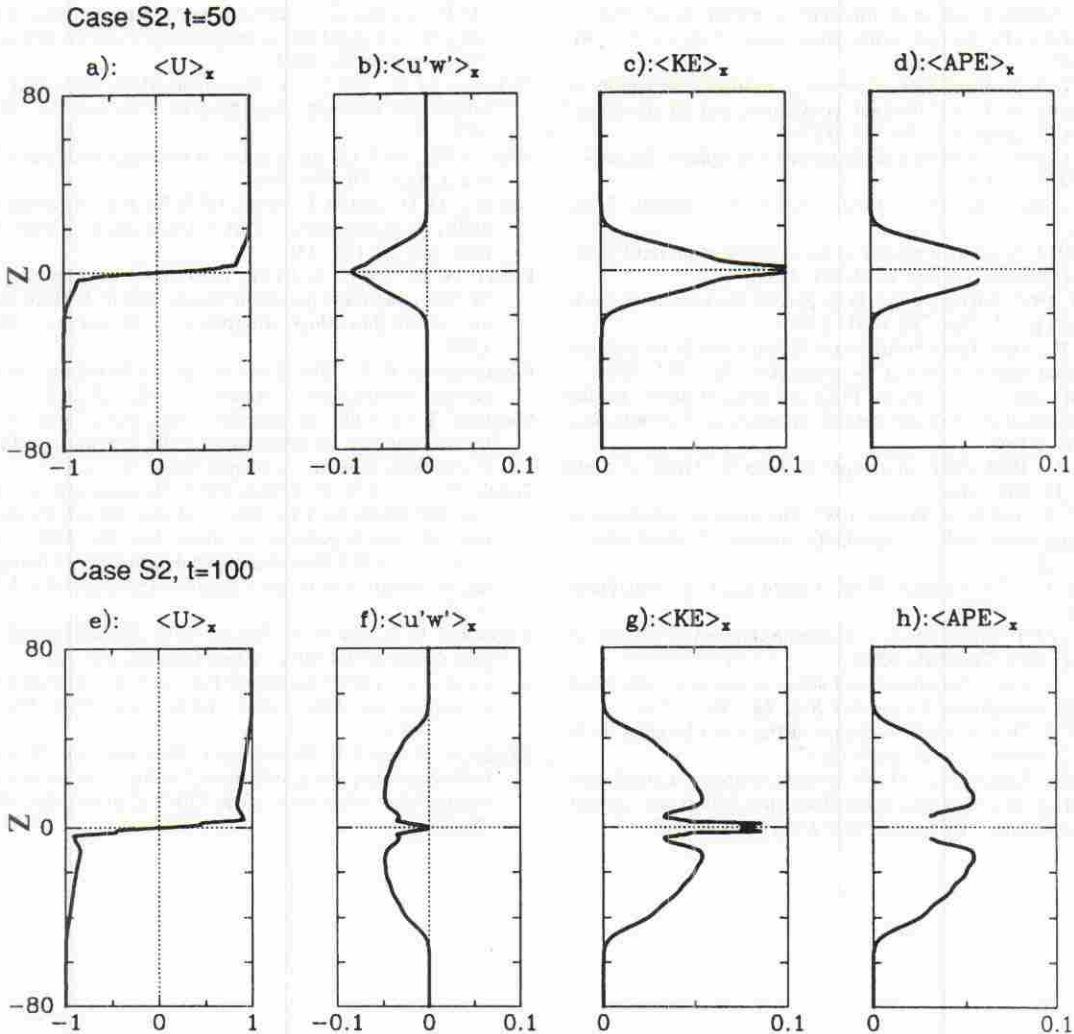
Case S2, t=50

Case S2, t=100

Fig. 13. From the shear simulation for $J = 1.0$ and $R = 5$ are shown vertical profiles at time $t = 50$ of (a) mean horizontal velocity, (b) Reynolds stress, (c) horizontally averaged wave kinetic energy, and (d) available potential energy. These four profiles are shown at time $t = 100$ in panels (e), (f), (g), and (h). The full vertical extent of the channel is shown in all eight panels and the horizontal scales are shown on each graph. APE is not shown for $|z| \leq R$ since this quantity may not be quadratic in ρ' over this range.

REFERENCES

Chimonas, G., and J. R. Grant, 1984: Shear excitation of gravity waves. Part II: Upscale scattering from Kelvin–Helmholtz waves. *J. Atmos. Sci.*, **41**, 2278–2288.

Clark, T. L., T. Hauf, and J. P. Kuettner, 1986: Convectively forced internal gravity waves: Results from two-dimensional numer-

ical experiments. *Quart. J. Roy. Meteor. Soc.*, **112**, 899–925.

Davis, P. A., and W. R. Peltier, 1979: Some characteristics of the Kelvin–Helmholtz and resonant overreflection modes of shear flow instability and of their interaction through vortex pairing. *J. Atmos. Sci.*, **36**, 2394–2412.

Drazin, P. G., and W. H. Reid, 1981: *Hydrodynamic Stability.* Cambridge University Press, 525 pp.

——, M. B. Zaturska, and W. H. H. Banks, 1979: On the normal modes of parallel flow of inviscid stratified fluid. Part 2. Unbounded flow with propagation at infinity. *J. Fluid Mech.*, **95**, 681–705.

Durran, D. R., and J. B. Klemp, 1987: Another look at downslope winds. Part II: Nonlinear amplification beneath wave overturning layers. *J. Atmos. Sci.*, **44**, 3402–3412.

Fovell, R., 1992: Numerical simulations of convectively generated stratospheric gravity waves. *J. Atmos. Sci.*, **49**, 1427–1442.

Fritts, D. C., 1982: Shear excitation of atmospheric gravity waves. *J. Atmos. Sci.*, **39**, 1936–1952.

——, 1984: Shear excitation of atmospheric gravity waves. Part II: Nonlinear radiation from a free shear layer. *J. Atmos. Sci.*, **41**, 524–537.

——, and G. D. Nastrom, 1992: Sources of mesoscale variability of gravity waves. Part II: Frontal, convective, and jet stream excitation. *J. Atmos. Sci.*, **49**, 111–127.

Geller, M. A., 1983: Dynamics of the middle atmosphere. *Space Sci. Rev.*, **34**, 359–375.

Gill, A. E., 1982: *Atmosphere–Ocean Dynamics.* Academic Press, 662 pp.

Hazel, P., 1972: Numerical studies of the stability of inviscid stratified shear flows. *J. Fluid Mech.*, **51**, 39–61.

Hines, C. O., 1960: Internal atmospheric gravity waves at ionospheric heights. *Can. J. Phys.*, **38**, 1441–1481.

Hodges, R. R., 1969: Eddy diffusion coefficients due to instabilities in internal gravity waves. *J. Geophys. Res.*, **74**, 4087–4090.

Holton, J. R., and R. S. Lindzen, 1972: An updated theory for the quasi-biennial cycle of the tropical stratosphere. *J. Atmos. Sci.*, **29**, 1076–1080.

Howard, L. N., 1961: Note on a paper by John W. Miles. *J. Fluid Mech.*, **10**, 509–512.

Klaassen, G. P., and W. R. Peltier, 1985: The onset of turbulence in finite-amplitude Kelvin–Helmholtz billows. *J. Fluid Mech.*, **155**, 1–35.

Lighthill, M. J., 1978: *Waves in Fluids.* Cambridge University Press, 504 pp.

Lilly, D. K., 1971: Observations of mountain-induced turbulence. *J. Geophys. Res.*, **76**, 6585–6588.

Lindzen, R. S., 1981: Turbulence and stress owing to gravity wave and tidal breakdown. *J. Geophys. Res.*, **86**, 9707–9714.

——, and J. R. Holton, 1968: A theory of the quasi-biennial oscillation. *J. Atmos. Sci.*, **25**, 1095–1107.

Lott, F., and H. Teitelbaum, 1992: Nonlinear dissipative critical level interaction in a stratified shear flow: instabilities and gravity waves. *Geophys. Astrophys. Fluid Dyn.*, **66**, 133–167.

——, H. Kelder, and H. Teitelbaum, 1992: A transition from Kelvin–Helmholtz instabilities to propagating wave instabilities. *Phys. Fluids A*, **4**, 1990–1997.

McIntyre, M. E., and M. A. Weissman, 1978: On radiating instabilities and resonant overreflection. *J. Atmos. Sci.*, **35**, 1190–1196.

Miles, J. W., 1961: On the stability of heterogeneous shear flows. *J. Fluid Mech.*, **10**, 496–508.

Nastrom, G. D., and D. C. Fritts, 1992: Sources of mesoscale variability of gravity waves. Part I: Topographic excitation. *J. Atmos. Sci.*, **49**, 101–110.

Peltier, W. R., and T. L. Clark, 1979: The evolution and stability of finite-amplitude mountain waves. Part II: Surface wave drag and severe downslope windstorms. *J. Atmos. Sci.*, **36**, 1498–1529.

Pierrehumbert, R. T., 1984: Local and global baroclinic instability of zonally varying flow. *J. Atmos. Sci.*, **41**, 2141–2162.

Shepherd, T. G., 1990: Symmetries, conservation laws, and Hamiltonian structure in geophysical fluid dynamics. *Advances in Geophysics*, Vol. 32, Academic Press, 287–338.

Smyth, W. D., and W. R. Peltier, 1989: The transition between Kelvin–Helmholtz and Holmboe instability: An investigation of the overreflection hypothesis. *J. Atmos. Sci.*, **46**, 3698–3720.

——, and ——, 1993: Two dimensional turbulence in homogeneous and stratified shear layers. *Geophys. Astrophys. Fluid Dyn.*, **69**, 1–32.

Sutherland, B. R., and W. R. Peltier, 1992: The stability of stratified jets. *Geophys. Astrophys. Fluid Dyn.*, **66**, 101–131.

——, and ——, 1994: Turbulence transition and internal wave generation in two dimensional stratified jets. *Phys. Fluids A*, **6**, 1267–1284.

Takahashi, M., and J. R. Holton, 1991: The mean zonal flow response to Rossby wave and gravity wave forcing in the equatorial lower stratosphere: relationship to the QBO. *J. Atmos. Sci.*, **48**, 2078–2087.